Geophysical Research Letters

RESEARCH LETTER
10.1029/2020GL090365

Shear Instability and Turbulence Within a Submesoscale Front Following a Storm

Jeffrey R. Carpenter[1], Arthur Rodrigues[1], Larissa K. P. Schultze[1], Lucas M. Merckelbach[1], Nobuhiro Suzuki[1], Burkard Baschek[1], and Lars Umlauf[2]

[1]Institute of Coastal Research, Helmholtz-Zentrum Geesthacht, Geesthacht, Germany, [2]Leibniz Institute for Baltic Sea Research, Warnemünde, Germany

Abstract Narrow baroclinic fronts are observed in the surface mixed layer (SML) of the Baltic Sea following an autumn storm. The fronts are subjected to hydrodynamic instabilities that lead to submesoscale and turbulent motions while restratifying the SML. We describe observations from an ocean glider that combines currents, stratification, and turbulence microstructure in a high horizontal resolution (150–300 m) to analyze such fronts. The observations show that SML turbulence is strongly modulated by frontal activity, acting as both source and sink for turbulent kinetic energy. In particular, a direct route to turbulent dissipation within the front is linked to shear instability caused by elevated nongeostrophic shear. The turbulent dissipation of frontal kinetic energy is large enough that it could be a significant influence in the evolution of the front and demonstrates that small-scale turbulence can act as a significant sink of submesoscale kinetic energy.

Key Points:
- An autonomous ocean glider observed turbulence, currents, and stratification in surface mixed layer submesoscale fronts following a storm
- Submesoscale fronts provide both a damping and generation of surface mixed layer turbulence
- Shear instability within the front could represent a significant energy transfer in frontal evolution

Supporting Information:
- Supporting Information S1

Correspondence to:
J. R. Carpenter,
jeff.carpenter@hzg.de

Citation:
Carpenter, J. R., Rodrigues, A., Schultze, L. K. P., Merckelbach, L. M., Suzuki, N., Baschek, B., & Umlauf, L. (2020). Shear instability and turbulence within a submesoscale front following a storm. *Geophysical Research Letters*, *47*, e2020GL090365. https://doi.org/10.1029/2020GL090365

Received 20 AUG 2020
Accepted 10 NOV 2020
Accepted article online 20 NOV 2020

1. Introduction

Ocean submesoscale motions are thought to provide an energetic link between the large, energy-containing mesoscales and small-scale turbulence where energy is dissipated (Ferrari & Wunsch, 2009; McWilliams, 2016). In the last decade, large resources have been devoted to observing such motions (Buckingham et al., 2019; Poje et al., 2014; Shcherbina et al., 2015), since they are known to be responsible for exerting controls on important processes such as primary production (Mahadevan, 2016; Taylor & Ferrari, 2011), pollutant dispersal (D'Asaro et al., 2018; Poje et al., 2014), and in the cascade of energy through the ocean general circulation (McWilliams, 2016). In this cascade, energy is input to the large [O(1,000–100 km)] basin scale and mesoscales but dissipated at the smallest turbulent scales [O(1 cm)], with the submesoscales thought to be at least partially responsible for bridging this gap. However, despite the intense observational efforts above, there remain few direct observations of small-scale turbulent energy transfers within submesoscale features. This is due to the challenges in measuring turbulence in such intermittent and rapidly evolving submesoscale flows. The few studies that have provided measurements of turbulent kinetic energy dissipation have focussed primarily on the intense and persistent western boundary current systems, such as the Gulf Stream (Thomas et al., 2016) and Kuroshio Current (D'Asaro et al., 2011; Nagai et al., 2009, 2012) and, more recently, also in dense eastern boundary upwelling filaments (Peng et al., 2020).

In this study, we describe measurements of submesoscale fronts during restratification of the surface mixed layer (SML) after the passage of a storm. The measurements quantify stratification, currents, and turbulent dissipation rates during and after the storm. To our knowledge, these are the first highly resolved turbulence observations within submesoscale fronts in the restratification phase following a storm. Measurements of turbulent dissipation during stormy conditions are rare (Schultze et al., 2020) and have been found to perturb submesoscale frontal activity in the SML, possibly leading to a loss of balance and a forward cascade of energy (Sullivan & McWilliams, 2018; Whitt & Taylor, 2017). The measurements were performed by an autonomous underwater glider equipped with microstructure shear sensors, as well as an acoustic current profiler and a conductivity-temperature-depth (CTD) system. This unique combination of sensors on a single autonomous platform allows for a quantification of the small-scale turbulent energy transfers, as well as the nongeostrophic current field, enabling an elucidation of the mechanisms forcing the frontal turbulence.

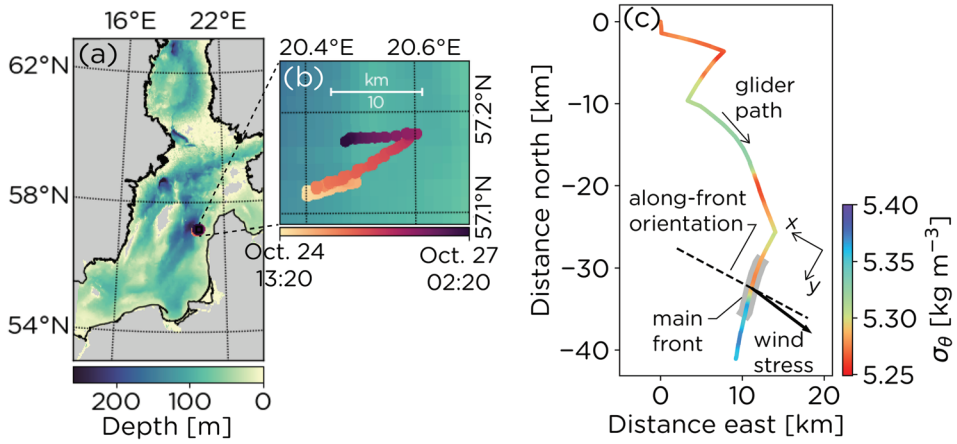

Figure 1. (a) Map of the measurement location in the Baltic Sea with the detailed glider surfacing positions along the transects shown in (b). The distance the glider swam through water, that is, the position relative to any advection by currents, is shown in (c). Colors in (c) represent the mean potential density anomaly, σ_θ, in the upper 5 m, and the gray shading indicates the position of the main front. Also shown in (c) are the estimated frontal orientation and the direction of the wind stress while the glider crossed the main front.

2. Study Area and Methods

The measurements took place between 20 and 28 October 2017, in the central Baltic Sea off the Latvian coast (Figure 1). The Baltic is known to experience frequent fronts in the SML due to a host of processes (Kahru et al., 1995). Only a subset of the collected data will be presented covering the period from 24 October at 13:20 to 27 October 02:20 (all times in Coordinated Universal Time, UTC, throughout), which coincides with the passing of a storm and the subsequent restratification of the SML. Measurements were performed using an autonomous underwater Slocum G2 shallow water glider programmed to dive between the near surface and depths between 65 and 75 m at dive and climb angles of ~26° to the horizontal. This flight results in an approximate horizontal resolution of twice the dive depth (i.e., 130–150 m) at the middepth of the dives, allowing for a submesoscale-resolving sampling of the SML. Despite the nearly east-west path of the glider relative to Earth (Figure 1b), strong northward directed currents resulted in a south oriented transect that the glider swam through water (Figure 1c). This path was determined by integrating the glider flight model of Merckelbach et al. (2019).

The glider was equipped with a Seabird SBE41 CTD sampling at 1 Hz and a Rockland Scientific MicroRider-1000 for the measurement of turbulence microstructure. From the MicroRider, data from two airfoil shear probes (512 Hz) are used to quantify the dissipation rate of turbulent kinetic energy, ϵ in W kg^{-1}. The methods used to arrive at ϵ involve extensive quality control and are described in detail in Schultze et al. (2017) but use the recent glider flight model of Merckelbach et al. (2019). More detail is in the supporting information.

In addition, data will be presented from a Teledyne RDI phased array 600 kHz Explorer Doppler Velocity Log (DVL) with ADCP capability. The glider-mounted downward looking DVL tracks the bottom and concurrently measures current profiles relative to the glider. The DVL was configured to measure 10 ping ensembles of 30 bins with a bin size of 1 m every 2–3 s. Multiple DVL ensembles were mapped into a single depth profile for each downcast, using the least squares optimization method described by Visbeck (2002) and extended in Todd et al. (2017). This allows for a quantification of currents only below a depth of 10 m due to insufficient data required in the bin averaging arising from the blanking distance of the DVL.

3. Results and Analysis

SML structure over the course of the storm is shown in Figure 2. This time period captures both the buildup and the relaxation phase of the wind stress, $\vec{\tau}_w$, with a peak magnitude of 1.0 N m^{-2}, corresponding to a 10 m wind speed of $U_{10} = 20$ m s^{-1}. The response of the SML to this forcing can be seen in the structure of the potential density field, ρ_θ, or equivalently $\sigma_\theta \equiv \rho_\theta - 1{,}000$ kg m^{-3} (Figure 2b). Prior to, and during, conditions

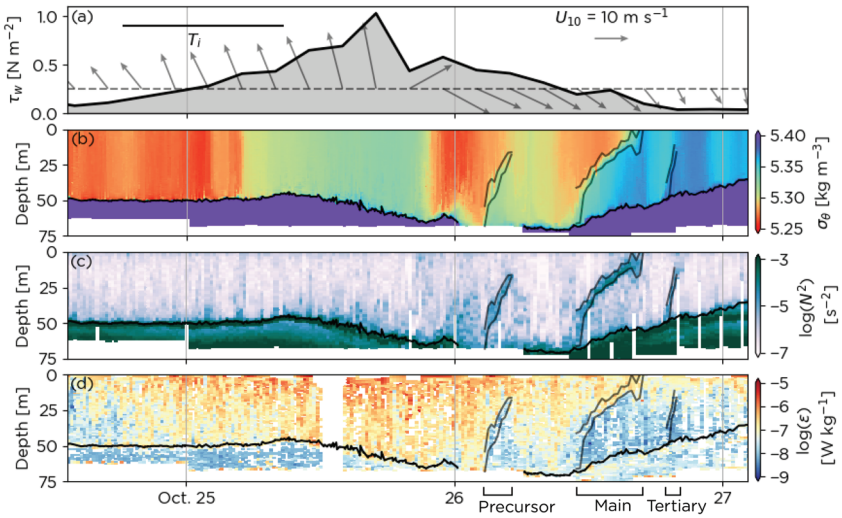

Figure 2. Structure of the surface mixed layer, including storm, and restratification periods. (a) Wind stress magnitude, τ_w, is shown by the filled line with 10 m wind speed vectors overlaid. Glider-based observations of (b) water potential density (σ_θ) with a color scale chosen to highlight SML variations, (c) squared buoyancy frequency of the sorted density profile, N^2, and (d) turbulent dissipation rate are plotted as time series. Frontal boundaries are indicated by the dark lines and correspond to the z_f^t and z_f^b positions discussed in the text. Sampling times of the three fronts are labeled at the bottom of (d). The base of the SML is indicated by the black line in (b–d). The horizontal bar in (a) indicates one inertial period, T_i = 14.3 hr.

of strong wind forcing, there is little vertical stratification observed within the SML, despite horizontal variations in σ_θ being present (Figures 2b and 2c during 25 October). Mean buoyancy gradients, calculated over the upper 40 m of the water column during the strongest winds, show that horizontal gradients are within an order of magnitude of vertical gradients (note that the random orientation of horizontal gradients relative to the glider path results in an underestimate). As the storm forcing relaxes, σ_θ is seen to exhibit sharp frontal structures where vertical stratification is concentrated (Figures 2b and 2c, gray lines). It is not known whether these were preexisting, or newly formed, fronts that the glider has sampled during the restratification phase. Three such fronts are outlined in Figures 2b–2d that will be referred to as the precursor, main, and tertiary fronts, in what follows. The upper and lower frontal boundary positions are denoted by z_f^t and z_f^b, respectively, and have been chosen in each dive profile of σ_θ to represent the region that stratification is confined to (Figures 2b, 2c, and 3a). In each case, the frontal boundaries capture greater than 90% of the total buoyancy jump across the front (see the supporting information for profiles and definitions within the main front).

Turbulence in the SML, measured by ϵ, is also seen to be strongly dependent on the storm forcing (Figure 2d), with a decay from values of approximately 10^{-6} W kg^{-1} close to the storm peak, to values closer to 10^{-8} W kg^{-1} during calm conditions. This turbulence is generally stronger near the surface where sources are present in the form of surface wave breaking and shear due to direct wind forcing. However, despite high levels of ϵ in the SML during the restratification phase (i.e., during 26 October), there is an influence exerted by the frontal structures on turbulence in the SML.

Closer inspection of the dissipation field in Figure 2d reveals that the stratified frontal regions (i.e., the regions between z_f^b and z_f^t) can also exhibit high levels of dissipation, evident within the main front above 25 m depth. The strong dissipation is seen to be vertically confined to the front (above z_f^b) and can even exhibit larger ϵ than in the SML above (see also Figures 3c and 4a). These observations suggest that a local generation mechanism may be present within the front. To explore this possibility further, we plot the detailed structure of the main front in Figure 3. As the glider measurements are a mix of both temporal and spatial variability, we have plotted the data with both relative time and cross-front distance scales. The stratification can be seen to be confined to within the frontal boundaries (Figure 3a, black lines corresponding to $z_f^{t,b}$) with the current taking the form of a frontal jet seen primarily on the upper flank of the front in Figure 3b. From these velocity measurements we define the total velocity difference across the front, $\Delta\vec{u}$, by averaging in the layer above z_f^t and below z_f^b, while still above the SML base and below 10 m depth.

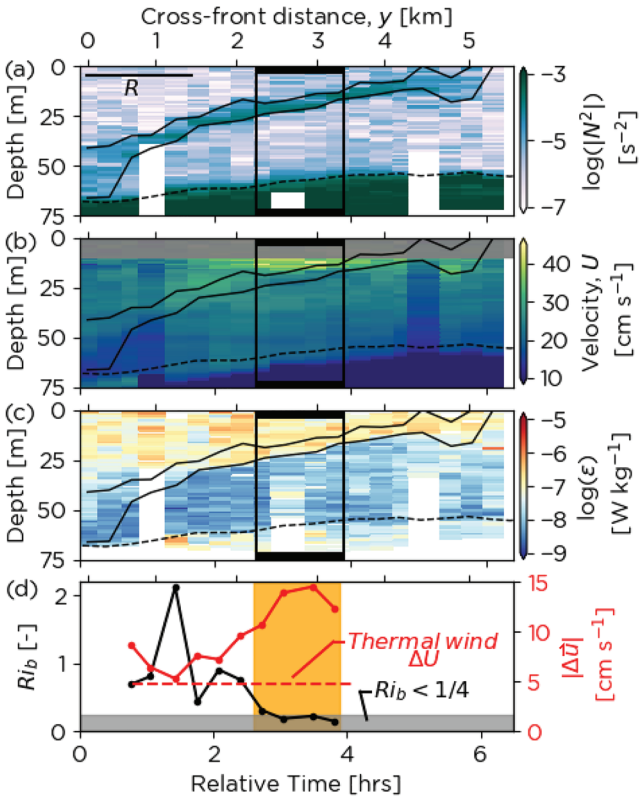

Figure 3. Spatial and temporal structure of the main turbulent SML front: (a) stratification measured through the absolute buoyancy frequency, $|N^2|$, (b) velocity in the along-front direction showing the frontal jet, (c) turbulence dissipation rate, and (d) bulk Richardson number and $|\Delta\vec{u}|$ across the front. The frontal boundaries ($z_f^{t,b}$) are indicated by dark lines and the base of the SML by a dashed line. The times of low Richardson numbers are indicated by the hollow boxes in (a–c) and the orange shading in (d). The condition $Ri_b < 1/4$ is represented by the gray shading in (d), with the mean thermal wind ΔU denoted by the red dashed line. The Rossby radius, $R \equiv (\Delta b\, H\,)^{1/2}/f$, is shown in (a). Only data from glider dives are shown, where DVL measurements were possible. Note the nonlinear cross-front distance axis. The second Ri_b data point from left in (d) was obtained by interpolating the z_f^b and Δb due to an incomplete glider dive profile.

The mean direction of $\Delta\vec{u}$ is taken as the frontal orientation so a mean crossing angle of the glider to the front can be defined, as well as an across-front distance, denoted by y (see Figure 1c). The velocities in Figure 3b are measured normal to this crossing angle of 78° ± 12° plus/minus one standard deviation (Figure 1c), with possible errors due to nongeostrophic currents not accounted for.

The presence of a frontal jet is to be expected when the front is in geostrophic balance. In this case we may approximate the *along-front* (opposed to the total) velocity difference, $|\Delta U|$, through the thermal wind balance by assuming a sharp two-layer stratification, giving $|\Delta U| = \Delta b s/f$, where $\Delta b \equiv g\Delta\rho/\rho_0$ is the buoyancy difference across the front, with $\Delta\rho$ the density difference across the front, $g = 9.8$ m s^{-2} the gravitational acceleration, $\rho_0 = 1{,}005$ kg m^{-3} a reference density, $f = 1.2\times10^{-4}$ s^{-1} the Coriolis frequency, and s the slope of the front. The assumption of a two-layer front is supported by the narrow thickness of the front relative to the mixed layer depth (with mean of 18%) or the narrow width of the front relative to its length—a feature that distinguishes it from many previously observed SML fronts (e.g., D'Asaro et al., 2011; Peng et al., 2020; Thomas et al., 2013, 2016).

The jet current strength based on across-front means of $\Delta b = 6.0\times10^{-4}$ m s^{-2} and $s = 9.7\times10^{-3}$ is shown in Figure 3d, together with $|\Delta\vec{u}|$. It can be seen that, especially near the core of the jet, the thermal wind prediction is considerably less than the observations. The frontal jet current strength therefore has a significant nongeostrophic component giving velocities up to threefold larger than mean thermal wind currents. Possible reasons for this discrepancy from geostrophy are discussed in the following section, along with the influence these large nongeostrophic velocities have on the turbulent structure of the front.

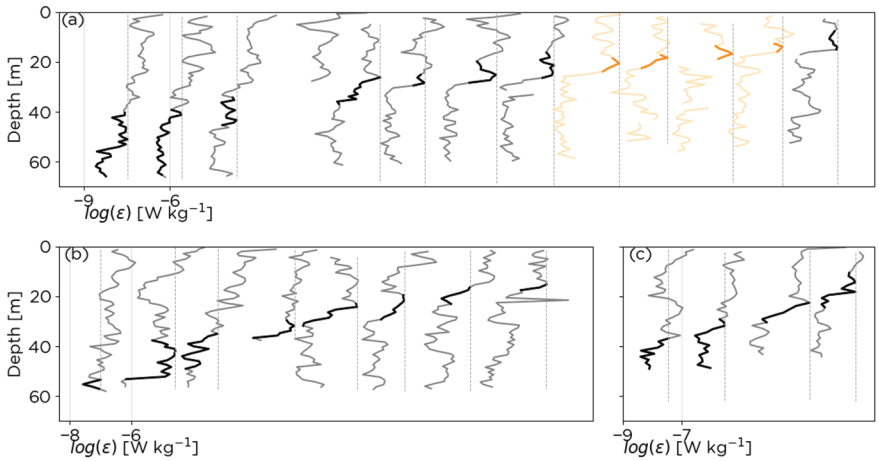

Figure 4. Profiles of the turbulent dissipation rate within the SML during glider dive transects of the three fronts following the storm. The main front is shown in (a), along with the precursor front (b) and the tertiary front (c). Thick dark regions of the curves indicated the frontal depths, with critical Ri_b profiles shown in orange. Each profile has been horizontally offset, with the maximum value of ϵ inside the front indicated by the dashed vertical line. The vertical resolution of the profiles corresponds to 98 cm, the vertical bin size for dissipation measurements.

4. Discussion

4.1. Influence of Fronts on SML Turbulence

As already noted, the fronts appear to exert an influence on the turbulent structure of the SML. Figure 4 shows profiles of ϵ measured in all fronts. A "sheltering" of the turbulence in the SML below the frontal stratification can be seen. On average, ϵ drops by more than an order of magnitude vertically across the fronts, corresponding to a drop of 6.6 times larger than that expected from law of the wall scaling. No coherent frontal current structure was identifiable from the DVL for the precursor and tertiary fronts. However, the turbulent structure within these fronts generally differs from that of the main front; the precursor and tertiary fronts appear to coincide with decreasing levels of turbulent dissipation (Figures 4b and 4c). This supports the lack of a turbulence generation mechanism within the precursor and tertiary fronts, wherein they act solely to damp turbulence generated at the near surface.

4.2. Shear Instability and Frontal Turbulence

A mechanism for turbulence generation within the main front can be understood by plotting the bulk Richardson number, defined as $Ri_b \equiv \Delta b h/|\Delta\vec{u}|^2$, where h is a length that is representative of the thickness of the layer of shear and stratification and is taken to be the vertical thickness of the front with $h \equiv |z_f^t - z_f^b|$. Ri_b will give a measure of the stability of the stratified frontal zone as a whole, effectively ignoring variability smaller than h within the front. Therefore, we do not use the current measurements from the DVL to evaluate the vertical shear, $S(z)$, in estimating a gradient Richardson number, $Ri_g(z) \equiv N^2/S^2$. This is due to (i) the need to reduce noise in the shear through layer averaging, (ii) uncertainties in the vertical structure of the shear layer that arise from bin averaging the DVL pings in a spatially nonuniform turbulent field, and (iii) the fact that for arbitrary stratified shear layers, $Ri_g(z)$, offers only a necessary condition for instability (Smyth & Carpenter, 2019).

As an alternative that overcomes the limitations of the DVL in assessing the fine vertical scales of the shear, we assume that the shear layer is centered on, and of the same vertical scale as, the frontal stratification. This appears generally consistent with the observations (see supporting information for a discussion) and results in a sufficient condition for instabilities of the Kelvin-Helmholtz type of $Ri_b < 1/4$, with sufficiently distant vertical boundaries (Carpenter et al., 2007; Smyth & Carpenter, 2019). This instability condition is satisfied within the central region of the frontal jet (indicated by boxes in Figures 3a–3c). With reference also to Figure 4, this region coincides with high dissipation levels observed within the front, and we therefore conclude that the strong nongeostrophic velocities are responsible for the generation of enhanced turbulence within much of the front through shear instability. Such a strong mixing process as Kelvin-Helmholtz instability is expected to rapidly alter the structure of the front and provides a direct energy pathway from submesoscale flows to small-scale turbulent dissipation through nongeostrophic shear.

Finally, we note that there are portions of the main front that could be susceptible to symmetric instabilities. However, the sensitivity of the (cyclonic) horizontal shear within the front in stabilizing the symmetric instability precludes definitive results (see supporting information for more details).

4.3. Dissipation of Frontal Energy

The turbulence dissipation measurements within the main front allow for an assessment of the potential role that small-scale turbulent energy transfers have in the evolution of the front. To carry out such an assessment, we define the kinetic energy of the front, E_K, through

$$E_K \equiv \int_0^{\ell_{10}} \int_{z_{ML}(y)}^{-10\,\mathrm{m}} \frac{\rho_0}{2} \left|\vec{u}(y,z) - \langle\vec{u}\rangle(y)\right|^2 \mathrm{d}z\mathrm{d}y, \tag{1}$$

where z is height (positive upwards) and the depth-mean current velocity

$$\langle\vec{u}\rangle(y) \equiv \frac{1}{-10 - z_{ML}(y)} \int_{z_{ML}(y)}^{-10\,\mathrm{m}} \vec{u}(y,z)\,\mathrm{d}z.$$

The integration limits in the above definitions are taken to range from $y = 0$, where the front meets the SML base, to $\ell_{10} = 3.6$ km, where the front meets 10 m depth, that is, the shallowest depth with reliable current measurements (Figure 3). Integration is performed in z between the base of the SML at z_{ML}, to 10 m depth. To correct for the unresolved frontal kinetic energy shallower than 10 m, we multiply by a correction factor given by the fraction of the total frontal area to the resolved area (to a depth of 10 m). The result of this calculation gives $E_K = 320$ kJ m^{-1} for the main front.

Given this E_K, we can use the measurements of ϵ to estimate a dissipation time scale for the frontal kinetic energy through $\tau \equiv E_K/D$. Here, D is the total dissipation (in W m^{-1}) within the frontal zone,

$$D \equiv \rho_0 \int_0^L \int_{z_f^b(y)}^{z_f^t(y)} \epsilon(y,z)\,\mathrm{d}z\mathrm{d}y,$$

with the total across-front length $L = 3.9$ km. Note that this estimate of D is likely a conservative underestimate, as it is only carried out on the dissipation profiles in which the front has not contacted the ocean surface, that is, those plotted in Figure 4a. The value obtained is $D = 3.1$ W m^{-1}, with 43% of this dissipation occurring in the shear unstable region. The resulting decay time scale for frontal kinetic energy is $\tau = 1.2$ days. This relatively short decay time indicates that the small-scale turbulent dissipation represents a potentially significant energy loss in the evolution of the front.

4.4. Departures From Geostrophy

Wind-driven Ekman transport—SML fronts are known to interact strongly with wind-driven currents (Thomas et al., 2013), through a modification of the geostrophic currents by Ekman transport. To estimate this influence within the main front, we compute the Ekman velocity expected from a given wind stress magnitude through $|\vec{V}_E| = |\vec{\tau}_w|/(\rho_0 f H_E)$, where H_E is the depth of the Ekman layer, taken to be the depth of high ϵ coincident with the bottom of the main front. This leads to an estimated mean Ekman velocity of $|\vec{V}_E| \approx 7$ cm s^{-1}, which is comparable to, but less than, the nongeostrophic component of 10 cm s^{-1} (see Figure 3d). However, given the orientation of the front and the wind stress (Figure 1c), we see that the Ekman transport is directed perpendicular to the front and in a stabilizing configuration, that is, from lighter to denser waters (90° to the right of the wind stress). If we account for this $\vec{V}_E$ in our definition of the front orientation, an along-front contribution of approximately 5 cm s^{-1} results. We would therefore not expect the wind-driven Ekman transport to result in the observed nongeostrophic along-front shear.

Frontal oscillations—During the storm, we expect that isopycnals in the SML will steepen through vertical mixing and upon relaxation of the storm forcing undergo geostrophic adjustment to a sloped configuration through SML restratification (Tandon & Garrett, 1994). Through this adjustment, frontal oscillations can be expected, and these oscillations can lead to altered currents and shear instabilities (Tandon & Garrett, 1994, 1995; Thomas et al., 2016). During a frontal oscillation, the front is expected to periodically steepen and flatten, while ΔU is reduced and enhanced, respectively. By assuming that potential vorticity (PV) in each layer i on either side of the front, $q_i \equiv (f - \mathrm{d}U_i/\mathrm{d}y)/h_i$, is conserved during such a process and that it consists entirely of planetary vorticity before the onset of restratification (i.e., $q_i = f/H$), it is possible to estimate an upper bound on the centerline jet velocity, $|\Delta U_{CL}| \equiv |U_1(L/2) - U_2(L/2)|$. Here we have used h_i to denote

the thickness of the ith layer and U_i its along-front velocity relative to the SML mean, with $0 \leq y \leq L$ the across-front coordinate and L the frontal length. The estimate is obtained by integrating the conservation of PV in each layer through the equations

$$\frac{dU_{1,2}}{dy} = f\left[1 - \frac{h_{1,2}(y)}{H}\right], \tag{2}$$

where the subscripts refer to the upper (1) and lower (2) layers of the front. The $|\Delta U_{CL}|$ is found once boundary conditions of $U_1(0) = U_2(L) = 0$ are supplied, and the difference in the layer velocities is taken. By assuming a fixed SML depth given by the mean, $H = 59$ m and taking the interface between the layers as the mean front depth [i.e., $(z_f^t + z_f^b)/2$], we can directly integrate (2) to give a $|\Delta U_{CL}| = 22$ cm s^{-1}. This value of the jet strength indicates that frontal oscillations could be sufficient to account for the strong nongeostrophic shear.

The equilibrium geostrophic adjustment solution for an initially vertical two-layer front with $q_i = f/H$, described by Csanady (1978), predicts a frontal length $L = 1.7R$, with $R \equiv (\Delta b\, H)^{1/2}/f$ the Rossby deformation radius (Figure 3). This predicted length of $L = 2.6$ km is roughly half that observed and would have a $|\Delta U_{CL}| = 15$ cm s^{-1}. Our observation of a longer front with greater jet strength than thermal wind therefore represents a departure from the geostrophic adjustment solution that is consistent with a frontal oscillation. In addition, we expect the oscillation period to be approximately the inertial period, $T_i = 14.2$ hr. Figure 2 therefore shows that the time between storm relaxation and the glider crossing of the front is sufficient for the development of shear from a frontal oscillation.

5. Summary and Conclusions

An autonomous ocean glider has been used to perform a high horizontal resolution (130–150 m) profiling of the ocean SML during, and immediately following, a storm. A series of three fronts was observed in the SML during the restratification phase. Collecting simultaneous measurements of currents, stratification, and the dissipation of turbulent kinetic energy, we find that the fronts can have a strong influence on all of these quantities. Although the fronts generally shelter and damp turbulence in the SML, they can also act as a source of turbulence through the formation of instabilities. The strongest of the three fronts was found to be susceptible to shear instability in a region that coincided with high dissipation rates. The source of the strong nongeostrophic shear is consistent with frontal oscillations. The energy dissipation levels were found to be significant and indicate that small-scale turbulent dissipation could be an important energy loss in frontal evolution.

Data Availability Statement

Glider data used in this study can be found online (http://www.doi.org/10.5281/zenodo.3992614), and the wind data from a reanalysis of the German Weather Service (DWD) are accessible through http://www.dwd.de/EN/ourservices/cdc/cdc.html website.

Acknowledgments
We would like to acknowledge financial support from the Helmholtz Association, as well as the German Research Foundation (DFG). Excellent support from the captain and crew of the Elisabeth Mann Borgese (cruise EMB169), as well as R. Kopetzky are also acknowledged. This paper is a contribution to project T2 of the Collaborative Research Centre TRR 181, "Energy Transfers in Atmosphere and Ocean," funded through DFG Grant 274762653.

References

Buckingham, C. E., Lucas, N. S., Belcher, S. E., Rippeth, T. P., Grant, A. L. M., Sommer, J. L., et al. (2019). The contribution of surface and submesoscale processes to turbulence in the open ocean surface boundary layer. *Journal of Advances in Modeling Earth Systems*, *11*, 4066–4094. https://doi.org/10.1029/2019MS001801

Carpenter, J. R., Smyth, W. D., & Lawrence, G. A. (2007). Evolution and mixing of asymmetric Holmboe instabilities. *Journal of Fluid Mechanics*, *582*, 103–132.

Csanady, G. T. (1978). Wind effects on surface to bottom fronts. *Journal of Geophysical Research*, *83*(C9), 4633–4640.

D'Asaro, E., Lee, C., Rainville, L., Harcourt, R., & Thomas, L. (2011). Enhanced turbulence and energy dissipation at ocean fronts. *Science*, *332*(6027), 318–322.

D'Asaro, E. A., Shcherbina, A. Y., Klymak, J. M., Molemaker, J., Novelli, G., Guigand, C. M., et al. (2018). Ocean convergence and the dispersion of flotsam. *Proceedings of the National Academy of Sciences*, *115*(6), 1162–1167. https://doi.org/10.1073/pnas.1718453115

Ferrari, R., & Wunsch, C. (2009). Ocean circulation kinetic energy: Reservoirs, sources and sinks. *Annual Review of Fluid Mechanics*, *41*, 253–281. https://doi.org/10.1146/annurev.fluid.40.111406.102139

Kahru, M., Hakansson, B., & Rud, O. (1995). Distributions of the sea-surface temperature fronts in the Baltic Sea as derived from satellite imagery. *Continental Shelf Research*, *15*, 663–679. https://doi.org/10.1016/0278-4343(94)E0030-P

Mahadevan, A. (2016). The impact of submesoscale physics on primary productivity of plankton. *Annual Review of Marine Science*, *8*, 161–84.

McWilliams, J. C. (2016). Submesoscale currents in the ocean. *Proceedings of the Royal Society*, *472*, 20160117.

Merckelbach, L. M., Berger, A., Krahmann, G., Dengler, M., & Carpenter, J. R. (2019). A dynamic flight model for Slocum gliders and implications for microstructure measurements. *Journal of Atmospheric and Oceanic Technology*, *36*, 281–296.

Nagai, T., Tandon, A., Yamazaki, H., & Doubell, M. J. (2009). Evidence of enhanced turbulent dissipation in the frontogenetic Kuroshio Front thermocline. *Geophysical Research Letters*, *36*, L12609. https://doi.org/10.1029/2009GL038832

Nagai, T., Tandon, A., Yamazaki, H., Doubell, M. J., & Gallager, S. (2012). Direct observations of microscale turbulence and thermohaline structure in the Kuroshio Front. *Journal of Geophysical Research*, *117*, C08013. https://doi.org/10.1029/2011JC007228

Peng, J.-P., Holtermann, P., & Umlauf, L. (2020). Frontal instability and energy dissipation in a sub-mesoscale upwelling filament. *Journal of Physical Oceanography*, *50*, 2017–2035.

Poje, A. C., Özgökmen, T. M., Lipphardt, B. L., Haus, B. K., Ryan, E. H., Haza, A. C., et al. (2014). Submesoscale dispersion in the vicinity of the deepwater horizon spill. *Proceedings of the National Academy of Sciences*, *111*(35), 12,693–12,698. https://doi.org/10.1073/pnas.1402452111

Schultze, L. K. P., Merckelbach, L. M., & Carpenter, J. R. (2017). Turbulence and mixing in a shallow shelf sea from underwater gliders. *Journal of Geophysical Research: Oceans*, *122*, 9092–9109. https://doi.org/10.1002/2017JC012872

Schultze, L. K. P., Merckelbach, L. M., & Carpenter, J. R. (2020). Storm-induced turbulence alters shelf sea vertical fluxes. *Limnology and Oceanography: Letters*, *5*, 264–270. https://doi.org/10.1002/lol2.10139

Shcherbina, A. Y., Sundermeyer, M. A., Kunze, E., D'Asaro, E., Badin, G., Birch, D., et al. (2015). The LatMix summer campaign: Submesoscale stirring in the upper ocean. *Bulletin of the American Meteorological Society*, *96*(8), 1257–1279.

Smyth, W. D., & Carpenter, J. R. (2019). *Instability in geophysical flows*. Cambridge, United Kingdom: Cambridge University Press.

Sullivan, P. P., & McWilliams, J. C. (2018). Frontogenesis and frontal arrest of a dense filament in the oceanic surface boundary layer. *Journal of Fluid Mechanics*, *837*, 341–380. https://doi.org/10.1017/jfm.2017.833

Tandon, A., & Garrett, C. (1994). Mixed layer restratification due to a horizontal density gradient. *Journal of Physical Oceanography*, *24*(6), 1419–1424.

Tandon, A., & Garrett, C. (1995). Geostrophic adjustment and restratification of a mixed layer with horizontal gradients above a stratified layer. *Journal of Physical Oceanography*, *25*(10), 2229–2241.

Taylor, J. R., & Ferrari, R. (2011). Ocean fronts trigger high latitude phytoplankton blooms. *Geophysical Research Letters*, *38*, L23601. https://doi.org/10.1029/2011GL049312

Thomas, L. N., Taylor, J. R., D'Asaro, E. A., Lee, C. M., Klymak, J. M., & Shcherbina, A. (2016). Symmetric instability, inertial oscillations, and turbulence at the Gulf Stream Front. *Journal of Physical Oceanography*, *46*(1), 197–217. https://doi.org/10.1175/JPO-D-15-0008.1

Thomas, L. N., Taylor, J. R., Ferrari, R., & Joyce, T. M. (2013). Symmetric instability in the Gulf Stream. *Deep Sea Research Part II: Topical Studies in Oceanography*, *91*, 96–110. Subtropical Mode Water in the North Atlantic Ocean.

Todd, R. E., Rudnick, D. L., Sherman, J. T., Owens, W. B., & George, L. (2017). Absolute velocity estimates from autonomous underwater gliders equipped with doppler current profilers. *Journal of Atmospheric and Oceanic Technology*, *34*(2), 309–333.

Visbeck, M. (2002). Deep velocity profiling using lowered acoustic doppler current profilers: Bottom track and inverse solutions. *Journal of Atmospheric and Oceanic Technology*, *19*(5), 794–807.

Whitt, D. B., & Taylor, J. R. (2017). Energetic submesoscales maintain strong mixed layer stratification during an autumn storm. *Journal of Physical Oceanography*, *47*(10), 2419–2427.